

Fabrication of the nitrogen doped ordered porous carbon derived from amino-maltose with excellent capacitance performance

Deyi Zhang^{1,2} · Mei Han¹ · Yubing Li¹ · Bing Wang¹ · Kunjie Wang¹ · Yi Wang¹ · Tiantian Yang¹ · Juanxia He¹ · Huixia Feng¹

Published online: 4 April 2017
© Springer Science+Business Media New York 2017

Abstract In this paper, pristine and nitrogen doped ordered porous carbon materials were fabricated by using maltose and amino-maltose synthesized by hydrothermal reaction as precursors via template strategy. The fabricated pristine ordered porous carbon (OPC) and nitrogen doped ordered porous carbon (NOPC) exhibit excellent textural properties and good capacitance performance, which specific surface area (S_{BET}) reach 1107 and 726 $\text{m}^2 \text{g}^{-1}$ for the pristine OPC and NOPC materials while the specific capacitance reach up to 139 and 183 F g^{-1} under a current density of 0.5 A g^{-1} , respectively. The capacitance retention rate for the pristine OPC and NOPC reaches ca. 81 and 92% as the current density increased from 0.5 to 20 A g^{-1} , and no apparent capacitance decrease was observed after 5000 cycles. Although a sharp decrease of specific surface area was observed after N doping, the specific capacitance of NOPC was improved about 31% than that of the pristine OPC, the enhanced wettability and surface availability after N doping were found to be responsible for the enhanced capacitance performance of NOPC.

Keywords Nitrogen doping · Ordered porous carbon · Amino-maltose · Capacitance performance

1 Introduction

Supercapacitors based on various carbon electrode materials with micro/nano-structure, such as graphene [1, 2], CNTs [3, 4], and porous carbons [5, 6], have attracted so much attentions in recent years due to their distinguished merits, such as the high power density, long cycle life, and better safety [1–6]. However, the low energy density of the supercapacitors greatly restricts their potential application [7]. So, improving the energy density of supercapacitors without sacrificing their excellent cycle life and high power density is a crucial challenge for researches.

Owing to the high surface areas, ordered porous structures and large pore volumes as well as the excellent chemical inertness and mechanical stability, ordered porous carbons (OPC) has been considered as an ideal electrode materials for supercapacitors [8, 9]. In recent years, it was reported that the heteroatoms doping (N, S, P or B) can further improve the capacitance performance of supercapacitors based on OPC electrodes [10–12]. In all of these heteroatoms, nitrogen is by far the most popular heteroatom for incorporating into the carbon matrix of OPC due to the enhanced wettability and conductivity of nitrogen doped OPC materials [6, 10, 12, 13]. Meanwhile, the pronounced pseudo-capacitance induced by N doping can apparently improve the charge storage capacity of OPC materials [6, 12, 14]. Thus, considerable attention has been given to the fabrication of N doped ordered porous carbons (NOPC). Recently, Lin et al. reported a N-doped mesoporous few-layer carbon, which specific capacitance reached up to 790 F g^{-1} [14]. Up to now, N doped ordered porous carbon could be obtained by two different strategies: (1) post-treatment doping by calcining pristine ordered porous carbon under ammonia-contained atmosphere; (2) in situ doping *via* carbonization of nitrogen rich precursors combining

✉ Deyi Zhang
lzdeyizhang@163.com

¹ College of Petrochemical Technology, Lanzhou University of Technology, Lanzhou 730050, China

² Key Laboratory of Eco-Environment-Related Polymer Materials of Ministry of Education, Northwest Normal University, Lanzhou 730070, China

with soft or hard template approach. The main drawback of the precursor strategy is less controllable in either the amount or distribution of the doped heteroatoms. In contrast, the latter approach allows a homogeneous incorporation of nitrogen atoms into the carbon matrix in a controlled fashion. For obtaining N doped ordered porous carbons with excellent textural properties and high doping content via template approach, the selection of the precursors is extremely important. Up to now, various nitrogen-enriched organics, such as yogurt [6], pyrrole [15], cyanamide [13], iron phthalocyanine [16] and urea [17], have been employed as precursors. Unfortunately, these organics always exhibit poor thermal-stability owing to the serious decomposition of C–N bond at high pyrolysis temperature, which would cause a sharp decrease of nitrogen content in the final products and destroy the architecture of carbon materials. So, it is difficult for researchers to get N doped ordered porous carbons with high doping content and excellent textural properties simultaneously.

In this paper, pristine and nitrogen doped ordered porous carbon with excellent textural properties and good capacitance performance were fabricated by using maltose or amino-maltose as precursors via template strategy. It should be noted that either the pristine ordered porous carbons using maltose as precursor or N doped ordered porous carbons using amino-maltose as precursor was rarely reported in the published literatures.

2 Experiment

2.1 Synthesis of the amino-maltose

The nitrogen enriched precursor amino-maltose was synthesized by hydrothermal method. In brief, 5.0 g of maltose was dissolved in 50 ml of 30 wt% ammonia water, and then the mixture solution was added in a 100 ml Teflon-lined stainless steel autoclave, and heated at 200 °C for 24 h. The obtained brown solution was dried in a vacuum oven at 105 °C for 48 h. After that, the dried product was ground into fine powder and used as a precursor for fabrication of the NOPC materials.

2.2 Fabrication of the nitrogen doped ordered porous carbon

The nitrogen doped ordered porous carbon NOPC was fabricated by employing a hard template approach. In brief, 1.0 g of the nitrogen-rich precursor was dissolved in a mixture solution of 1.0 ml of alcohol and 0.1 ml of 98 wt% H₂SO₄, and then the solution was slowly dropped onto the surface of 1.0 g of SBA-15 template. The impregnated template was heated at 80 °C for 2 h under vacuum to evaporate

alcohol and then carbonized under an argon atmosphere at 800 °C for 2 h. Finally, the silica template was removed in a HF (10 wt%) aqueous solution to obtain the final materials.

2.3 Fabrication of the pristine ordered porous carbon

The pristine ordered porous carbon OPC also was obtained via a similar hard template approach. Briefly, 1.5 g of maltose and 0.2 ml of 98% H₂SO₄ was dissolved in 5 ml of H₂O, and then 1 g of SBA-15 was added to above mixture solution. The mixture was heated at 105 °C for 6 h and then pre-carbonized at 150 °C for 6 h under atmosphere. The dark brown product was then carbonized under 800 °C for 2 h under Ar atmosphere followed by treating with HF (10 wt%) aqueous solution and washing with 95% ethanol and distilled water. After drying in vacuum oven at 105 °C for 6 h, the pristine ordered porous carbon was obtained.

2.4 Material characterization

The X-ray photoelectron spectroscopy (XPS, Thermo Multilab 2000 instrument) with Al *ka* excitation source was employed to determine the element compositions and their chemical environment. The small-angle X-ray scattering (SAXS) measurements were taken on a X'Pert X-ray diffractometer (Phillips). The *d* spacing values were calculated by the formula $d = \lambda / 2 \sin \theta$, and the unit cell parameters were calculated from the formula $a = 2 \times 3^{-1/2} d_{100}$. The wall thickness was calculated from $W_T = a - D$, where *a* represents the unit cell parameter and *D* is the pore diameter calculated from the N₂ sorption measurements. The specific surface areas and pore distribution of the fabricated materials were measured by a Micromeritics ASAP 2020 volumetric adsorption analyzer at 77 K. Before the measurements, the samples were evacuated under vacuum ($p < 10^{-5}$ mbar) at 373 K. The morphology was investigated by means of scanning electron microscope (SEM, Hitachi S-4800) and transmission electron microscope (TEM, JEM-2010).

2.5 Electrochemical measures

Symmetric supercapacitor cells were assembled using the fabricated OPC and NOPC as electrode materials and 6 mol l⁻¹ KOH solution as electrolyte. To prepare the electrodes, the OPC or NOPC was ground with acetylene black (10 wt%) and polytetrafluoroethylene (PTFE, 10 wt%), and then pressed onto nickel foam that served as a current collector. The electrodes fitted with the separator (PP/PE complex film) and electrolyte solution were symmetrically assembled into electrode/separator/electrode construction (sandwich-type cells). Cyclic voltammetry (CV) was performed on a CHI 660E electrochemical analyzer (Shanghai,

Table 1 Element compositions of the amino-maltose precursor, pristine OPC and NOPC materials

Samples	C at%	N at%	O at%
Amino-maltose	66.8	15.9	17.3
OPC	94.67	–	5.33
NOPC	89.9	6.2	3.9

China). The galvanostatic charge/discharge and cycle-life stability were tested using a computer controlled supercapacitor testing system (NEWARE 5V0.1A, Shenzhen China). The specific discharge capacitance ($F g^{-1}$) for a single electrode was calculated using the following formula:

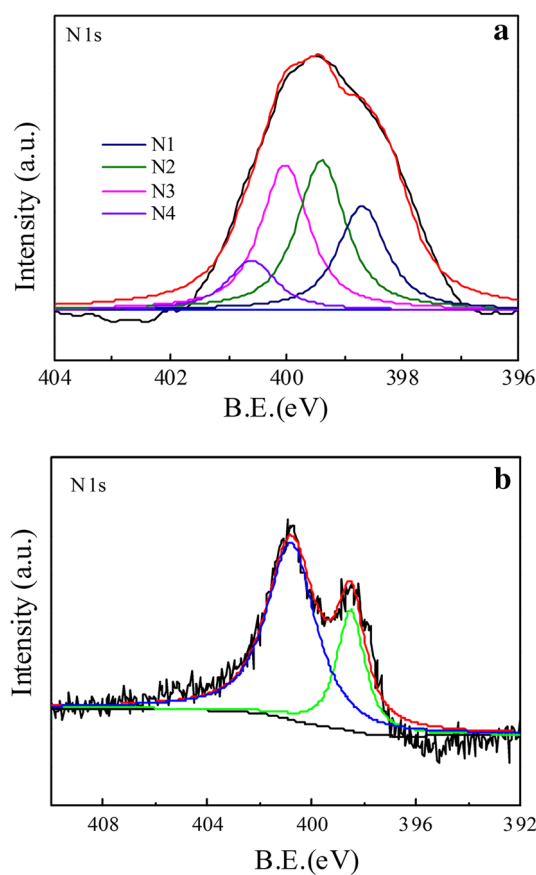
$$C_m = \frac{4(I \times \Delta t)}{\Delta V \times m} \quad (1)$$

where I refers the applied current density (A), Δt and ΔV present the discharging time (s) and potential range after the IR drop (V), and m (g) is the total mass of electrodes.

3 Results and discussion

The element composition of the amino-maltose precursor and the fabricated OPC and NOPC materials was analyzed by XPS. As shown in Table 1, C, N and O were found to be the main elements for the amino-maltose precursor and the fabricated NOPC, and no N element was found for the pristine OPC. The N-rich nature of the amino-maltose precursor was presented by the high N content of up to 15.9 at.%. Beside the C and N elements, abundant of O element also was detected in amino-maltose precursor (over 17.3 at.%), indicating that a lot of $-OH$ groups in maltose molecules still were reserved after treating by ammonia water under hydrothermal condition. These $-OH$ groups play a crucial role for the formation of the stable carbon framework in the future carbonization process via intermolecular dehydration reaction catalyzed by hot concentrate H_2SO_4 . The sharp decrease of O content during the carbonization process presented a reasonable evidence for this speculation, and the similar O content for NOPC and pristine OPC samples also provides an another evidence. On the other hand, the N doping content of the NOPC was much lower than that of the amino-maltose precursor, indicating the serious pyrolysis of C–N bonds during the carbonization process. Even so, the N doping content for the NOPC sample still reached 6.2 at.%, indicating the high N doping nature of the fabricated NOPC materials.

The XPS also was employed to detect the chemical environment of the N heteroatoms in both precursor and NOPC samples. As shown in Fig. 1 a, the N1s orbit of the N-rich precursor exhibited a higher complexity, which showed

**Fig. 1** XPS spectra of N1s orbit for the amino-maltose precursor and the fabricated NOPC material

several peaks at 398.2 (N1), 399.6 (N2), 400.1 (N3) and 400.5 (N4) eV. The peaks around 398.2 and 400.5 eV can be assigned to the amino functional groups located on the phenyl ring or carbon chain [18, 19] while the peaks at 399.6 and 400.1 eV were considered to be originated from a mixture of imine and non-protonated amine groups [20, 21]. After carbonization, N-containing functional groups converted to the carbon-bound N species. On the other hand, the N1s orbital of the NOPC sample exhibited two peaks at 398.4 and 400.6 eV, respectively. The peak located at 398.4 eV can be assigned to the pyridinic-like N species which were bound to two carbon atoms and donates one p electron to the aromatic π system, while another peak located at 400.6 eV commonly attributed to the quaternary N species bound within a graphite-like framework, which were incorporated into the graphene layer and replaced a carbon atom within a graphene plane [22–24]. It has been proved that the pyridinic-like N species located at the edges of the graphene layers possess high physical and chemical activity due to the strong attraction for the electrolyte ions, and contributed to generate pseudocapacitance for N doped carbon materials [19]. The relative content of the

Fig. 2 Nitrogen adsorption–desorption isotherms (a) and the pore size distributions (b) of the NOPC and pristine OPC materials

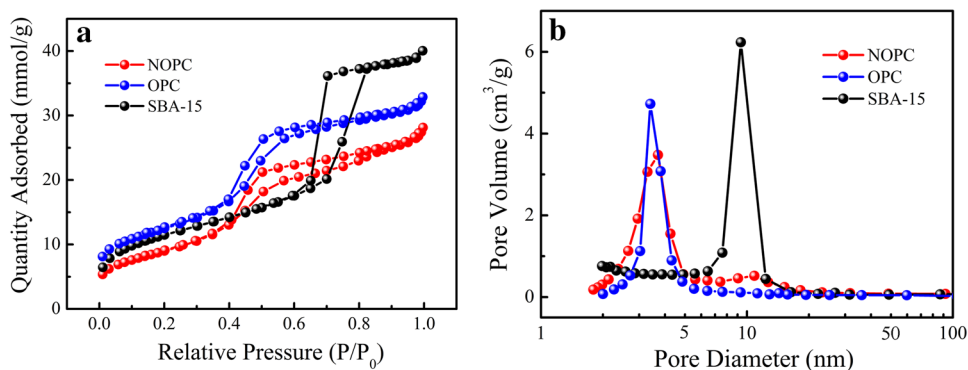


Table 2 Textural parameters of the fabricated NOPC and pristine OPC materials

Sample ID	d_{100}/nm	a/nm	D_p/nm	D_{av}/nm	W_T/nm	$S_{BET}/\text{m}^2 \text{g}^{-1}$	$V_T/\text{cm}^3 \text{g}^{-1}$	$V_M/\text{cm}^3 \text{g}^{-1}$
SBA-15	9.50	10.97	6.58	6.73	4.39	930	1.44	1.34
OPC	8.33	9.62	3.40	3.94	6.09	1107	1.35	1.27
NOPC	7.95	9.18	3.70	4.32	5.48	726	1.02	1.01

D_p Pore diameter, D_{av} Average pore diameter

pyridinic-like N species in the NOPC sample is over more than 28.2%, which would be favourable for the electrochemical performance of the presented materials.

The nitrogen adsorption–desorption isotherms and the pore size distributions of the fabricated NOPC, pristine OPC and the template SBA-15 were presented on the Fig. 2, and the textural parameters of the corresponding samples were presented in Table 2. As shown in Fig. 2a, the nitrogen adsorption/desorption isotherms of the fabricated NOPC and pristine OPC samples exhibited representative type IV adsorption isotherms with apparent H1 hysteresis loop at relative pressure from 0.4 to 0.9, which was the typical characteristic of the mesoporous materials. The similar nitrogen adsorption/desorption isotherms with the SBA-15 template indicated the ordered mesoporous structure of NOPC and pristine OPC samples like that of the SBA-15. However, the initial step of hysteresis loop of NOPC and pristine OPC samples shifted to the lower relative pressure comparing with that of SBA-15 template, implying a lower pore size than that of the SBA-15 template [25]. The NOPC and pristine OPC samples exhibited a similar initial position for hysteresis loop and slope for the adsorption branches, indicating the identical pore structure for the NOPC and pristine OPC samples. Figure 2b exhibited the pore size distribution curves of the NOPC and OPC samples. As shown in Fig. 2b, all samples exhibited a narrow pore size distribution, indicating the uniform pore size of NOPC and OPC samples. The pore size of the NOPC and pristine OPC was about 3.70 and 3.43 nm, respectively. The slight increase for pore size after N doping maybe due to the structure defects induced by the N heteroatoms doping. Even so, the pore size of the NOPC and pristine

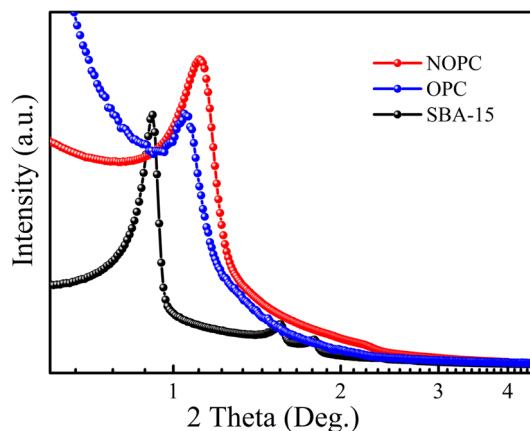


Fig. 3 SAXS patterns of the NOPC and pristine OPC materials

OPC samples was very near the pore wall thickness of SBA-15 template (4.39 nm), indicating that the NOPC and pristine OPC samples successfully reversely duplicate the pore structure of the ordered mesoporous silicon molecular sieve SBA-15. The fabricated NOPC and pristine OPC materials exhibited high specific surface area and large pore volume. As shown in Table 2, the S_{BET} of the NOPC and pristine OPC materials reached 726 and 1107 $\text{m}^2 \text{g}^{-1}$, respectively. Meanwhile, pore volume reached up to 1.02 and 1.35 $\text{cm}^3 \text{g}^{-1}$ for NOPC and pristine OPC materials, respectively. The sharp decrease for S_{BET} and pore volume after N doping indicated that the N heteroatom caused partial destruction for the pore structure.

Figure 3 presented the SAXS patterns of the NOPC and pristine OPC samples. As shown in Fig. 3, the SAXS

patterns of NOPC and pristine OPC samples exhibited a similar shape as SBA-15 template. Three diffraction peaks, associated with 100, 110, and 200 reflections of 2D hexagonal symmetry with the space group of $p6mm$, can be recognized clearly [13, 26]. Meanwhile, the shift of diffraction peaks to higher angle than that of the SBA-15 template indicated the framework shrinkage during the pyrolysis/carbonization process of the precursor. As shown in Table 2, the cell parameter (a) of the NOPC and pristine OPC samples were calculated to be 9.18 and 9.62 nm, both of which were lower than that of SBA-15 template (10.97 nm). The lower cell parameter (a) of the NOPC than that of pristine OPC illuminated that N doping aggravated the framework shrinkage during the pyrolysis/carbonization process.

Figure 4 displayed the typical SEM and TEM images of the fabricated NOPC and pristine OPC materials. As shown in Fig. 4a, b, the fabricated NOPC and pristine OPC samples exhibited the similar kernel-like morphology with a uniform diameter of about 500 nm. The TEM images of the NOPC and pristine OPC materials apparently presented the well-ordered mesoporous structure. The uniform stripe-like and hexagonally arranged images of the 2D hexagonal symmetry with the space group of $p6mm$ can be observed clearly. Meanwhile, the pore size of the NOPC and pristine

OPC materials estimated from the TEM images were ca 4 nm, it was very close to the pore wall thickness of SBA-15 template (4.39 nm). All of these results demonstrated that the fabricated NOPC and pristine OPC materials have truly reversely replicated the morphology and pore structure of the SBA-15 template.

The capacitive performance of the two-electrode symmetrical supercapacitor cell based on the fabricated NOPC (SC-NOPC) and pristine OPC (SC-OPC) electrodes was evaluated using best-practice methods with 6 M KOH as electrolyte. As shown in Fig. 5a, the cyclic voltammetry (CV) curves of SC-NOPC and SC-OPC exhibited a good symmetrically rectangular shapes in the potential range from 0 to 1 V under a scan rate of 5 mV s^{-1} , illuminated the ideal electrochemical double-layer (EDL) capacitance nature [27, 28]. Meanwhile, the symmetrically rectangular shapes of CV curves still were well maintained under a high scan rate of 200 mV s^{-1} (as shown in Fig. 5b), indicating the excellent power capability of the fabricated NOPC and OPC electrode materials. Even so, the CV curves area of SC-NOPC was higher than that of the SC-OPC, indicating the high charge storage/release capability of the SC-NOPC than that of the SC-OPC. The galvanostatic charge–discharge curves of the SC-NOPC and SC-OPC under current

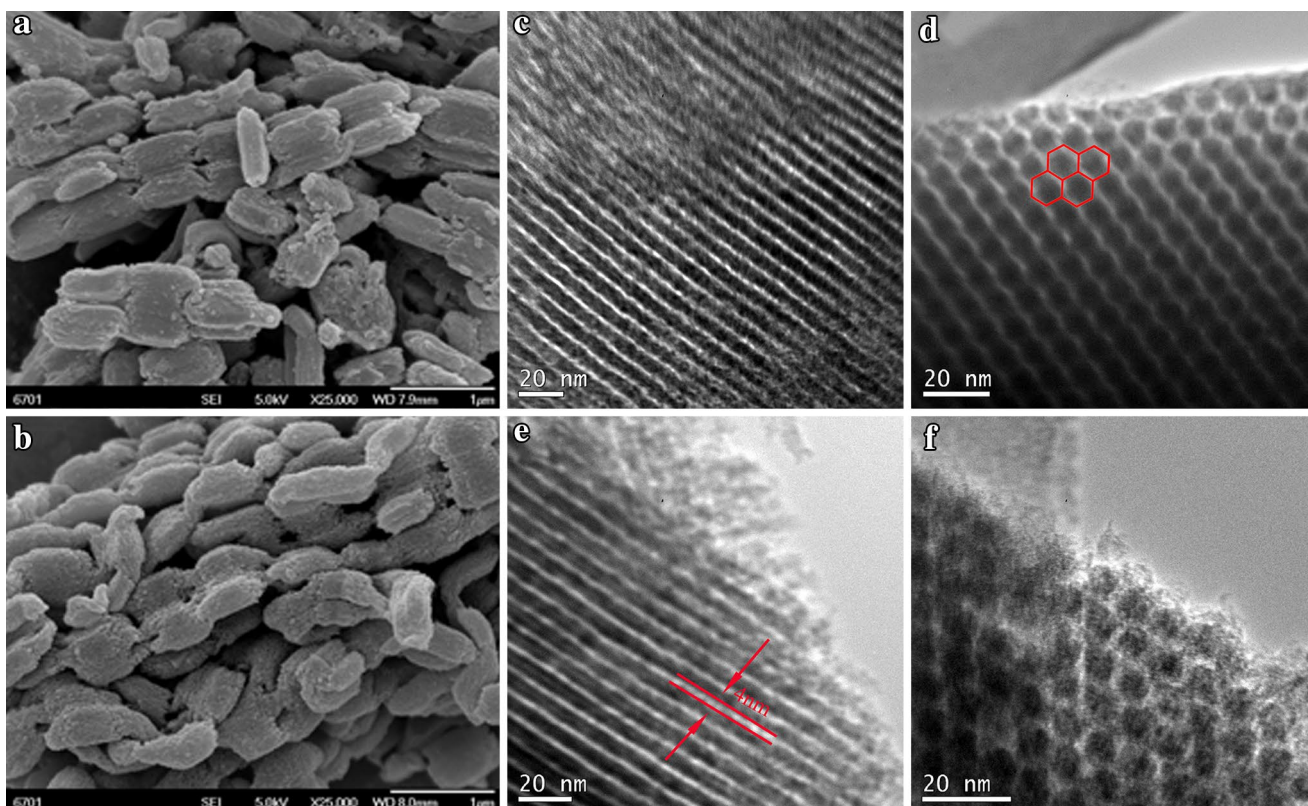


Fig. 4 Typical SEM images of the pristine OPC (a) and NOPC (b) materials; typical TEM images of the pristine OPC (c and d) and NOPC (e and f) materials

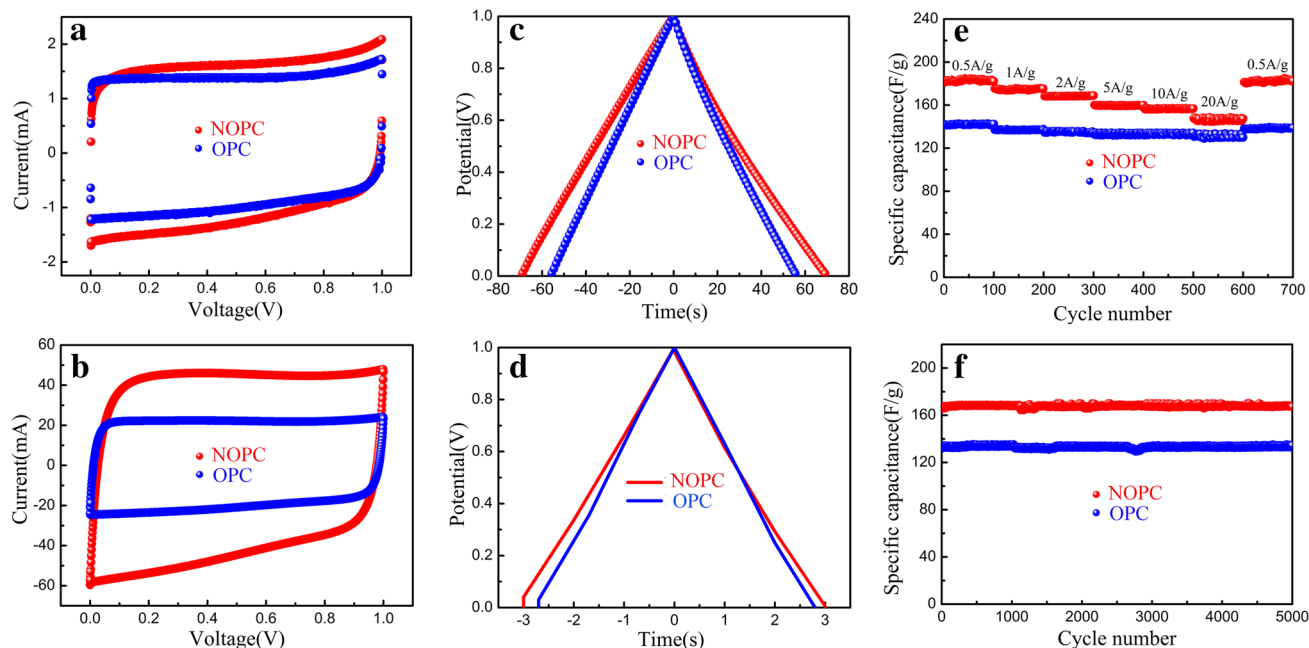


Fig. 5 CV curves of the NOPC and pristine OPC electrodes at a scan rate of 5 (a) and 200 mV s^{-1} (b); galvanostatic charge/discharge curves of the NOPC and pristine OPC electrodes at a current density of 1 (c) and 20 A g^{-1} (d); the effect of the current density on the

capacitance of the NOPC and pristine OPC electrodes (e); the cycling performance of NOPC and pristine OPC electrodes at a current density of 2 A g^{-1} (f)

density of 1 and 20 A g^{-1} were presented on Fig. 5c, d. As shown in Fig. 5c, d, all tested cells exhibited a triangular charge–discharge curves with a coulombic efficiency of nearly 100% even under a high current density of 20 A g^{-1} , illuminated the excellent EDL capacitance performance for the tested cells again. No apparent IR drop (voltage drop) was observed as a current density of 1 A g^{-1} for SC-NOPC and SC-OPC cells, illuminating a low ESR in the test cells. Under high current density of 20 A g^{-1} , only a very little IR drop of ca. 0.015 V was observed for SC-NOPC cell, and no apparent IR drop was observed for SC-OPC cell, demonstrating the lower ESR for SC-OPC cell than that of the SC-NOPC cell. N heteroatoms doping partially destroyed the well-ordered porous structure, and caused the sharp decrease for specific surface area. Even so, the NOPC electrode exhibited a higher specific discharge capacitance than that of the OPC electrode. As shown in Fig. 5e, the specific capacitance value of the NOPC electrode reached 183 F g^{-1} under a current density of 0.5 A g^{-1} while that of the pristine OPC electrode only reached 139 F g^{-1} . Although the specific surface area of NOPC only reached 66% of the pristine OPC, the specific capacitance of NOPC electrode was higher about 31% than that of the pristine OPC. The improved charge storage/release capability of the NOPC electrode than that of the pristine OPC electrode maybe due to the enhanced surface wettability induced by the N doping, which improved the surface area availability of NOPC

electrode, and then enhanced the charge storage/release capability of electrode materials [29]. The good rate capability of the NOPC and OPC electrodes also was presented on Fig. 5e. As shown in Fig. 5e, the specific capacitance of NOPC electrode slowly decreased from 183 to 148 F g^{-1} as the current density increased from 0.5 to 20 A g^{-1} while that of the pristine OPC electrode slowly decreased from 139 to 128 F g^{-1} . Although the capacitance retention rate of NOPC electrode (ca. 81%) was lower than that of the pristine OPC electrode (ca. 92%), the capacitance of NOPC electrode was still higher than that of the OPC electrode even under high current density. Moreover, all of the NOPC and OPC electrodes exhibited excellent cycle stability, as shown in Fig. 5f, no apparent capacitance reduction was observed for NOPC and OPC electrodes after 5000 cycles, and the capacitance retention rate reached nearly 100%.

4 Conclusion

The pristine and nitrogen doped ordered porous carbon materials were successfully fabricated by using maltose or amino-maltose as precursors via template strategy. The S_{BET} and the total pore volume reached 1107 $\text{m}^2 \text{g}^{-1}$ and 1.35 $\text{cm}^3 \text{g}^{-1}$ for the pristine OPC while those of the NOPC reached 726 $\text{m}^2 \text{g}^{-1}$ and 1.02 $\text{cm}^3 \text{g}^{-1}$. Although the NOPC with a N doping content of 6.2 at% exhibited

a lower S_{BET} value due to the structure defects induced by N doping, the capacitance of NOPC was higher about 31% than that of the pristine OPC. The capacitance of NOPC reached up to 183 F g^{-1} while that of the pristine OPC only reached 139 F g^{-1} under a current density of 0.5 A g^{-1} . The enhanced wettability and surface availability after N doping were found to be responsible for the improved capacitance performance of NOPC. The high capacitance retention rate of ca 81 and 92% for NOPC and pristine OPC as the current density increases from 0.5 to 20 A g^{-1} indicated the good rate capability of the reported materials. Meanwhile, the excellent cycle stability of the fabricated NOPC and pristine OPC also were presented by the near 100% capacitance retention rate after 5000 cycles.

Acknowledgements This work was supported by the National Natural Science Foundation of China (Grant No. 51462020); the Key Laboratory of Eco-Environment-Related Polymer Materials of the Ministry of Education Program (Grant No. KF-13-01); the Foundation for Innovation Groups of Basic Research in Gansu Province (Grant No. 1606RJA322); the Hongliu young teacher cultivate project of Lanzhou University of Technology (Grant No. Q201112).

References

1. Y. Shao, M.F. El-Kady, L.J. Wang, Q. Zhang, Y. Li, H. Wang, M.F. Mousavi, R.B. Kaner, *Chem. Soc. Rev.* **44**(11), 3639–3665 (2015)
2. J. Yu, J. Wu, H. Wang, A. Zhou, C. Huang, H. Bai, L. Li, *ACS Appl. Mater. Interfaces* **8**(7), 4724–4729 (2016)
3. D.P. Dubal, N.R. Chodankar, Z. Caban-Huertas, F. Wolfart, M. Vidotti, R. Holze, C.D. Lokhande, P. Gomez-Romero, *J. Power Sources* **308**, 158–165 (2016)
4. D.T. Pham, T.H. Lee, D.H. Luong, F. Yao, A. Ghosh, V.T. Le, T.H. Kim, B. Li, J. Chang, Y.H. Lee, *ACS Nano* **9**(2), 2018–2027 (2015)
5. X. Xu, Y. Liu, M. Wang, C. Zhu, T. Lu, R. Zhao, L. Pan, *Electrochim. Acta* **193**, 88–95 (2016)
6. M. Wahid, G. Parte, D. Phase, S. Ogale, *J. Mater. Chem. A* **3**(3), 1208–1215 (2015)
7. N. Goubard-Bretesché, O. Crosnier, F. Favier, T. Brousse, *Electrochim. Acta* **206**, 458–463 (2016)
8. E. Lim, C. Jo, J. Lee, *Nanoscale* **8**(15), 7827–7833 (2016)
9. G. Hasegawa, K. Kanamori, T. Kiyomura, H. Kurata, T. Abe, K. Nakanishi, *Chem. Mater.* **28**(11), 3944–3950 (2016)
10. Y. Deng, Y. Xie, K. Zou, X. Ji, *J. Mater. Chem. A* **4**(4), 1144–1173 (2016)
11. J. P. Paraknowitsch, A. Thomas, *Energy Environ. Sci.* **6**(10), 2839–2855 (2013)
12. D. Zhang, L. Zheng, Y. Ma, L. Lei, Q. Li, Y. Li, H. Luo, H. Feng, Y. Hao, *ACS Appl. Mater. Interfaces* **6**(4), 2657–2665 (2014)
13. Q. Shi, R. Zhang, Y. Lv, Y. Deng, A.A. Elzatahrya, D. Zhao, *Carbon* **84**, 335–346 (2015)
14. T.-Q. Lin, F.-X. Liu, C.-Y. Yang, H. Bi, F.-F. Xu, F.-Q. Huang, *Science* **350**(6267), 1508–1513 (2015)
15. K. Wan, G.-F. Long, M.-Y. Liu, L. Du, Z.-X. Liang, P. Tsiakaras, *Appl. Catal. B* **165**, 566–571 (2015)
16. D.-S. Yang, D. Bhattacharjya, M.Y. Song, F. Razmjooei, J. Ko, Q.-H. Yang, J.-S. Yu, *ChemCatChem* **7**, 2882–2890 (2015)
17. Z. Wang, Y. Li, X.-J. Lv, *RSC Adv.* **4**(107), 62673–62677 (2014)
18. P.M. Dietrich, N. Graf, T. Gross, A. Lippitz, S. Krakert, B. Schüpbach, A. Terfort, W.E.S. Unger, *Surf. Interface Anal.* **42**(6–7), 1184–1187 (2010)
19. C. Guimon, A. Gervasini, A. Auroux, *J. Phys. Chem. B* **105**(42), 10316–10325 (2001)
20. X. Song, Y. Ma, C. Wang, P.M. Dietrich, W.E.S. Unger, Y. Luo, *J. Phys. Chem. C* **116**(23), 12649–12654 (2012)
21. N. Graf, E. Yegen, T. Gross, A. Lippitz, W. Weigel, S. Krakert, A. Terfort, W.E.S. Unger, *Surf. Sci.* **603**(18), 2849–2860 (2009)
22. X. Xu, Y. Li, Y. Gong, P. Zhang, H. Li, Y. Wang, *J. Am. Chem. Soc.* **134**, 16987–16990 (2012)
23. R. Liu, D. Wu, X. Feng, K.M. Ilen, *Angew. Chem. Int. Ed.* **49**, 2565–2569 (2010)
24. Y. Xia, R. Mokaya, *Adv. Mater.* **16**(17), 1553–1558 (2004)
25. Z. Lei, Y. Xiao, L. Dang, M. Lu, W. You, *Microporous Mesoporous Mater.* **96**, 127–134 (2006)
26. M. Zhang, A. Sun, Y. Meng, L. Wang, H. Jiang, G. Li, *Microporous Mesoporous Mater.* **204**, 210–217 (2015)
27. C. Vix-Guterl, S. Saadallah, K. Jurewicz, E. Frackowiak, M. Reda, J. Parmentier, J. Patarin, F. Beguin, *Mater. Sci. Eng.* **108**(1–2), 148–155 (2004)
28. Z.-Y. Li, M.S. Akhtar, O.B. Yang, *J. Alloys Compd.* **653**, 212–218 (2015)
29. K. Gong, F. Du, Z. Xia, M. Durstock, L. Dai, *Science* **323**, 760–764 (2009)